ARTICLE

Check for updates

# Summertime low clouds mediate the impact of the large-scale circulation on Arctic sea ice

Yiyi Huang[1], Qinghua Ding [2✉], Xiquan Dong [1], Baike Xi[1] & Ian Baxter[2]

The rapid Arctic sea ice retreat in the early 21st century is believed to be driven by several dynamic and thermodynamic feedbacks, such as ice-albedo feedback and water vapor feedback. However, the role of clouds in these feedbacks remains unclear since the causality between clouds and these processes is complex. Here, we use NASA CERES satellite products and NCAR CESM model simulations to suggest that summertime low clouds have played an important role in driving sea ice melt by amplifying the adiabatic warming induced by a stronger anticyclonic circulation aloft. The upper-level high pressure regulates low clouds through stronger downward motion and increasing lower troposphere relative humidity. The increased low clouds favor more sea ice melt via emitting stronger longwave radiation. Then decreased surface albedo triggers a positive ice-albedo feedback, which further enhances sea ice melt. Considering the importance of summertime low clouds, accurate simulation of this process is a prerequisite for climate models to produce reliable future projections of Arctic sea ice.

[1] Department of Hydrology and Atmospheric Sciences, University of Arizona, Tucson, AZ, USA. [2] Department of Geography, and Earth Research Institute, University of California, Santa Barbara, Santa Barbara, CA, USA. ✉email: qinghua@ucsb.edu

Observations show a substantial decline in Arctic sea ice at alarming rates over the past few decades[1–3], raising a growing concern that the Arctic climate has shifted to a new normal. The sea ice is melted by various dynamical and thermodynamical processes. Among them, clouds could play an important role through their interactions with the ocean and sea ice[4–7]. Of particular significance are Arctic low clouds (cloud top height <3 km), which are a key climate feature of the atmospheric boundary layer over the Arctic Ocean during summer[8,9]. Arctic low clouds are important because they have strong influence on the amount of solar and infrared radiation[10], thus affecting the ice melting rate. In addition, low cloud variability can strongly modify the low-level heat, moisture, and momentum fluxes that sea ice is most sensitive to[9].

Previous studies demonstrate that there exists an active coupling between clouds and sea ice in early spring. In late spring and summer, clouds become more sensitive to large-scale circulation and thus may more actively drive sea ice variations[5,11,12]. Specifically, a strong upper-level barotropic anticyclone over the Arctic is found to be able to warm the lower troposphere by adiabatic descent in summer (June, July, August; JJA) during the period of 1979–2014 (ref. [12]). Some studies suggest that warm and dry conditions associated with the strong barotropic high pressure lead to reduced cloudiness and enhanced downwelling shortwave (SW) radiation. The increase in solar radiation leads to more ice melt, or indirectly enhances basal ice melt by heating the ocean surface[13–15]. On the other hand, it is speculated that this anomalous high-pressure system could create conditions conducive for increased low cloud amount, which leads to more longwave (LW) radiative flux at the surface to melt sea ice[7,12,16]. Although the statistical relationship between summertime large-scale circulation and clouds is significant, it is difficult to sort out the causal relationship as these processes are closely coupled together. The main hurdle to understand these underlying processes is that current climate models have a limitation to fully reproduce observed large-scale circulation variability with increasing greenhouse gas emissions[12], possibly due to models' incapability to simulate teleconnections between the tropics and high latitudes[17], and relatively low model resolution[18].

To make progress, here we use two novel approaches including: (I) a fingerprint analysis to focus on those subperiods of a long integration of model simulations when the observed circulation patterns are successfully reproduced; and (II) nudging experiments in which observed winds in the Arctic are imposed in a climate model. The main goal of this study is thus to gain a more comprehensive understanding of how large-scale atmospheric circulation variability regulates changes in low clouds, as well as the important role of low clouds in modulating sea ice melt versus that induced by anthropogenic forcing in summer. Since reliable cloud observations are available after 2000, we focus on the 17-year period from 2000 to 2016, during which sea ice experienced the most significant changes in the past four decades.

Results

Observed relationships between the clouds, circulation, and Arctic sea ice. A previous study has demonstrated the strong linkage between summertime large-scale circulation and September sea ice variations over the Arctic[12]. It shows that the decline of September sea ice concentration (SIC) is preceded by increasing pan-Arctic geopotential height at 200 hPa (Z200) in JJA from 2000 to 2016 (Fig. 1a), with a strong negative correlation $r = -0.68$. Specifically, the JJA Z200 has been rising over northeastern Canada, Greenland, and northeastern Eurasia (Fig. 1b), while September SIC has been retreating over the Beaufort, Chukchi, and East Siberian Seas (Fig. 1c). In the

meantime, the NASA Clouds and Earth's Radiant Energy System (CERES) satellite product[19] shows that JJA low cloud fraction (CF > 700 hPa) has been generally increasing over the Arctic Ocean (Fig. 1d). The most prominent changes are found over the Beaufort and Chukchi Seas, the region hereafter defined as the area of focus (AOF, 71°–80°N, 162°–222°) in this study. These increased low clouds are mainly liquid-containing clouds, with the largest positive trend occurring below ~920 hPa, which has been confirmed by both active remote sensing product Cloud-Aerosol Lidar and Infrared Pathfinder Satellite Observation (CALIPSO; Supplementary Fig. 1) and ERA-Interim reanalysis (hereafter ERA-I, Supplementary Fig. 2). In contrast to ice clouds, Arctic liquid-containing clouds generally have higher optical depths and a larger influence on surface LW radiation[20]. Therefore, the downwelling LW (LW_down) cloud radiative effect (CRE) at the surface has been increasing over the marginal seas in summer, particularly over the AOF (Fig. 1e). Note that the surface LW_down flux has also been increasing over the Arctic Ocean, except over the Canadian Archipelago, and its linear trend is most likely attributable to low clouds, with the largest contribution over the AOF (Supplementary Fig. 3).

To better demonstrate the relationships between circulation, clouds, and sea ice, we applied maximum covariance analysis (MCA) to objectively determine the primary coupled patterns between upper-level circulation and low clouds in summer. As shown in Fig. 1f, the leading MCA mode (MCA1) for the JJA Z200 time series is significantly correlated ($r = 0.79$) with JJA low CF. We then calculated correlations of MCA1 JJA low CF time series with SIC from June to September. The strongest negative correlations occur over the Beaufort, Chukchi, and East Siberian Seas in August and September (Fig. 1g), suggesting that increasing JJA low CF may lead to subsequent sea ice decline potentially because of enhanced LW CRE. Note that the correlation patterns do not show substantial changes with detrended data (Supplementary Fig. 4). We also find significant positive correlations between low clouds and SIC in the northern Canadian Archipelago. In summer, the SW flux also plays an important role in controlling sea ice melt. The downwelling SW (SW_down) flux has been reduced (Supplementary Fig. 5) because of an increase in low clouds and a reduction in surface albedo. On the one hand, the increased low CF may reflect more incoming solar radiation and reduce the SW flux transmission[13,21,22]. On the other hand, the surface albedo has been decreasing with sea ice melt, which substantially reduces the multiple reflections between surface and clouds[23]. In the meantime, the upwelling SW flux is substantially reduced with a much larger magnitude as a result of decreased SW_down flux and surface albedo, thus leading to an increase in absorbed solar radiation (Supplementary Fig. 5). Therefore, we believe that the increased low clouds enhance the ice melt that in turn trigger the pan-Arctic ice-albedo feedback.

Next, we explore the key mechanisms to link large-scale atmospheric circulation and low cloud variability. Figure 2 provides additional details about the summertime atmospheric state during the period 2000–2016. The low-level vertical structures of temperature and humidity over the AOF suggest that both temperature and humidity inversions exist <900 hPa (Fig. 2a, b), while the relative humidity (RH) decreases with height (Fig. 2c). The increased Z200 associated with the anticyclonic circulation aloft is found to be highly correlated with summertime vertical motion in the lower troposphere[12], mainly confined within the AOF. Therefore, stronger downward motion at 500 hPa occurs over the AOF (Fig. 2e). In principal, the subsidence is thought to inhibit the vertical growth of cloud layer by warming and drying the atmosphere. However, when there is a humidity inversion above cloud top, the subsidence would
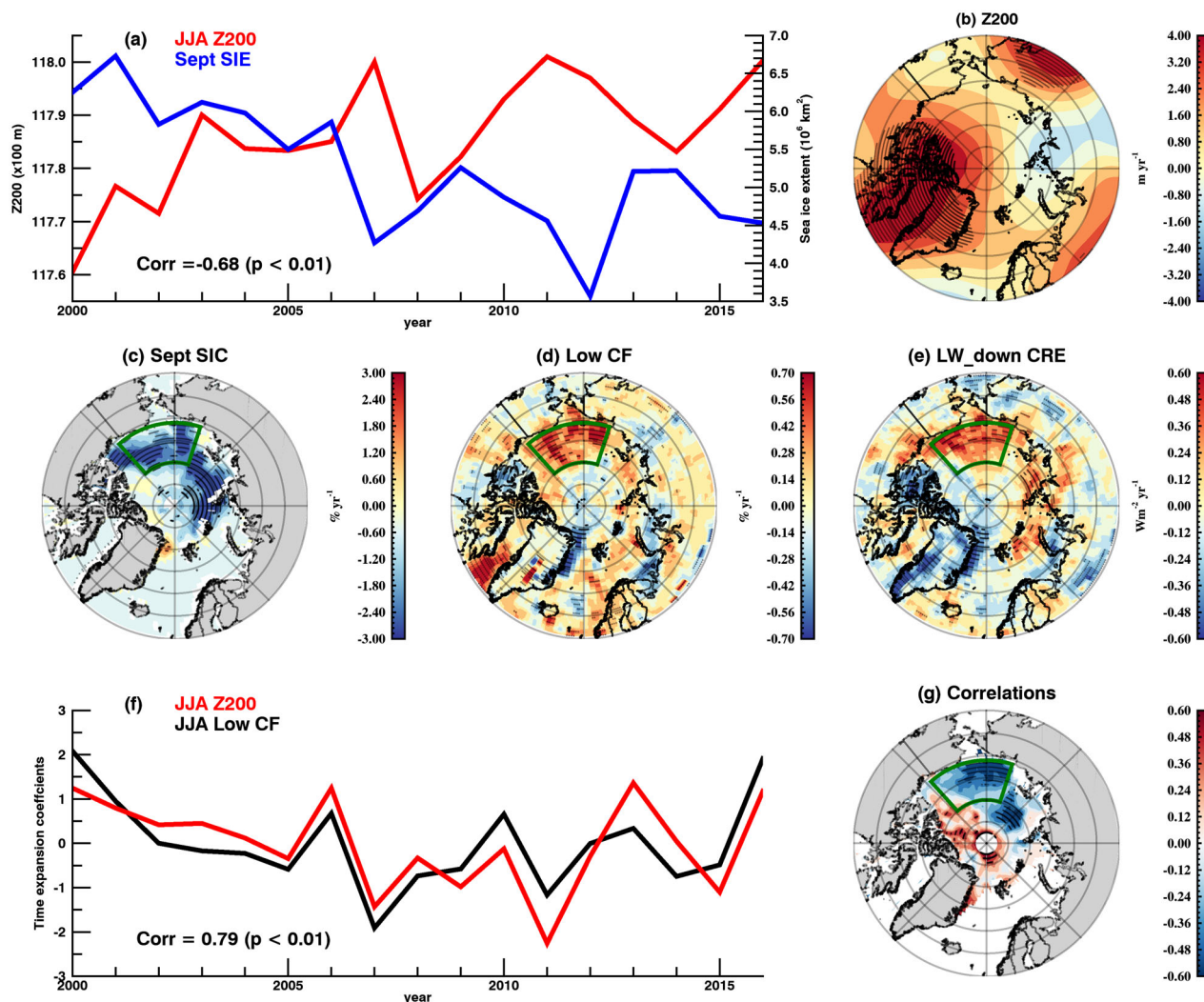
Fig. 1 Relationships between the summertime low clouds, large-scale circulation, and September Arctic sea ice during 2000–2016. a Time series of JJA geopotential height at 200 hPa (Z200) in the Arctic north of 60˚N and September Arctic sea ice extent (SIE). **b** Linear trend of JJA Z200 in ERA-I. **c** Linear trend of September sea ice concentration in NSIDC passive microwave sea ice product. **d** Linear trend of JJA low cloud fraction (CF, <700 hPa) in CERES SYN1deg Ed4.1 satellite product. **e** Linear trend of JJA downwelling longwave (LW_down) cloud radiative effect (CRE) at the surface in CERES-EBAF Ed4.1 satellite product. **f** Leading mode time series of JJA Z200 and low CF obtained from maximum covariance analysis, which accounts for 49.6% of the covariance of two variables. **g** Correlations between September sea ice concentration and leading mode time series of low-level CF. The black dots indicate statistically significant linear trends at 10% significance level. The green box in **c**, **d**, **e** and **g** marks the area with the most significant increasing trend of JJA low CF. This area is defined as area of focus (AOF, 71˚–80˚N, 162˚–222˚) in this study.

transport moisture into the cloud layer, which facilitates the formation and maintenance of clouds[9]. In the Arctic, both temperature and humidity inversions are prevalent, especially the coincidence of both inversions near the cloud top. They can serve as a moisture source for cloud formation and this mechanism has been confirmed by various previous studies based on long-term ground-based observations[24], aircraft observations[9], field campaigns[25], and model simulations[26]. Therefore, due to the coexistence of humidity and temperature inversions along with stronger downward motion, RH has been increasing <875 hPa over the AOF (Fig. 2f). The enhanced RH leads to increases in clouds below ~925 hPa, with the largest trend at ~975 hPa. In addition to vertical motion, the advection also plays a crucial role for Arctic summertime low stratiform clouds[9,27,28]. Enhanced poleward moisture transport at 950 hPa is found from the Laptev Sea to central Arctic Ocean during 2000–2016 (Supplementary Fig. 6). The stratus clouds could result from the

influx of warm and moist air from subpolar latitudes into the Arctic Basin[27]. Previous studies suggest that clouds in the Beaufort Sea that form in this situation tend to have relatively low cloud bases[29]. Moreover, the transport of aerosol particles might also be important for Arctic low cloud formation[30]. Note that no summer cloud response to sea ice loss is found in either observations[5] or model simulations[31,32]. In summer, a weaker air–sea temperature gradient occurs with a melting sea ice surface, resulting in a more stable atmosphere, which limits the turbulent flux exchange and thus reduces the cloud formation[5,27,33].

The spatial patterns shown in Fig. 2g, h indicate that the most prominent inversions occur over the Beaufort, Chukchi, and East Siberian Seas, with the greatest intensities around ~3 K and ~0.4 g kg^{-1} for temperature and humidity inversions, respectively. Moreover, the largest positive trend (~0.5% year^{-1}) of RH is found over the North Atlantic Ocean and Norwegian Sea, as well
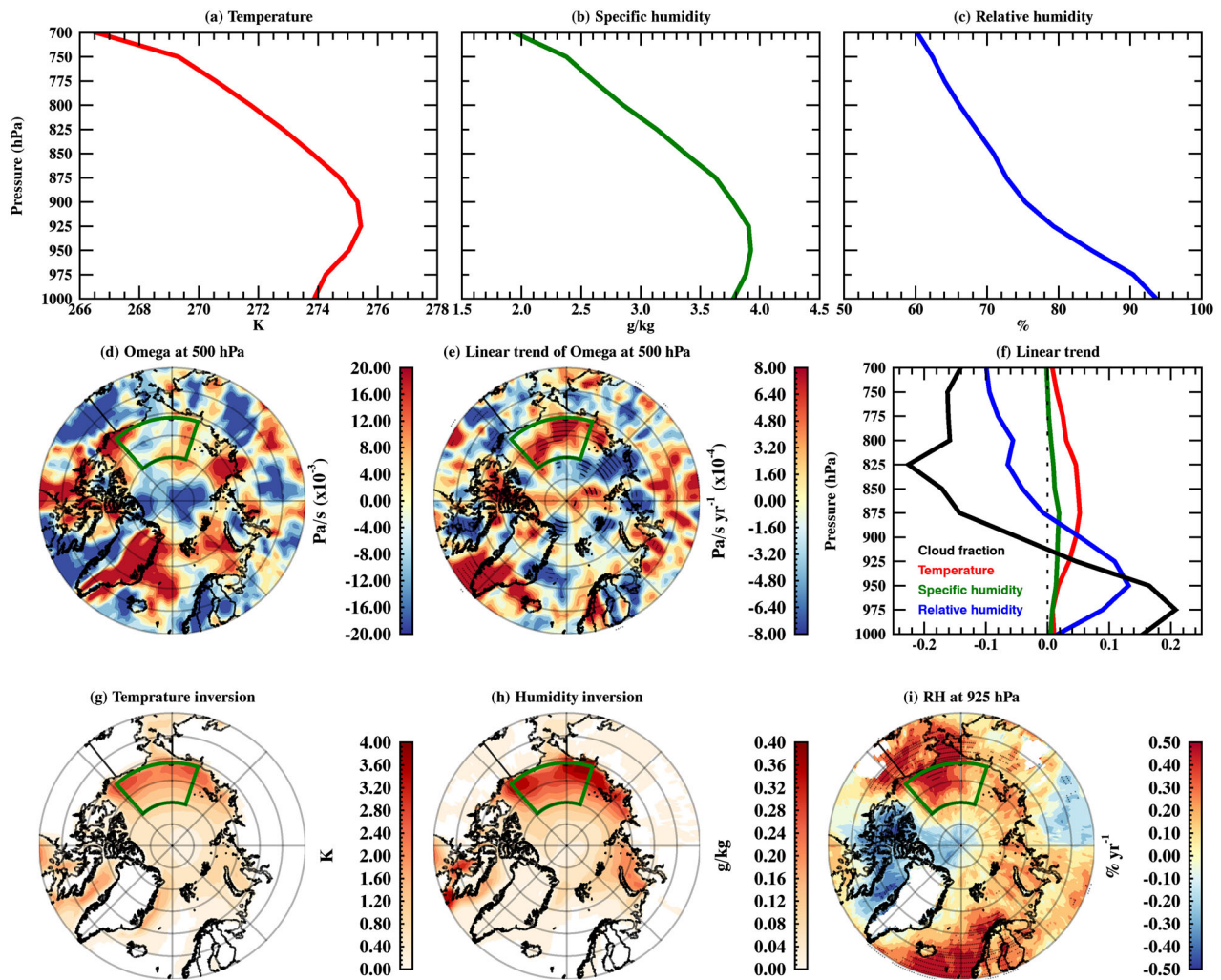
Fig. 2 The mechanisms responsible for increasing summertime low clouds during 2000–2016 over the Arctic. a Vertical structure of average JJA air temperature over the AOF (71°–80°N, 162°–222°) in ERA-I. **b** Vertical structure of average JJA specific humidity over the AOF in ERA-I. **c** Vertical structure of average JJA relative humidity (RH) over the AOF in ERA-I. **d** Average JJA vertical velocity (omega) at 500 hPa in ERA-I (positive values represent downward motion). **e** Linear trend of JJA vertical velocity (omega) at 500 hPa in ERA-I. **f** Vertical structure of JJA linear trend of thermodynamical parameters over the AOF in ERA-I. **g** Average JJA temperature inversion intensity <900 hPa in ERA-I. **h** Average JJA humidity inversion intensity <900 hPa in ERA-I. **i** Linear trend of JJA RH at 925 hPa in NASA AIRS satellite product. The black dots indicate statistically significant linear trends at the 10% significance level. The green box in **d**, **e**, **g–i** marks the area with the most significant increasing trend of JJA low CF. This area is defined as area of focus (AOF, 71°–80°N, 162°–222°) in this study.

as Beaufort and Chukchi Seas. The latter shows a substantial increasing trend of low-level liquid-containing clouds.

Overall, a plausible mechanism, based upon the observational analysis, could operate such that increased JJA low clouds, which may be strongly affected by upper-level atmospheric circulation, enhance the LW_down flux and reduce the SW_down flux at the surface. This leads to further sea ice decline and the newly open water then allows more solar heating of the upper ocean. In this case, the summertime low clouds could play an important role in modulating sea ice variations by bridging the large-scale circulation and surface.

Simulated relationships between the clouds, circulation, and Arctic sea ice. To examine whether a climate model is capable of capturing the observed features, we analyze model output from the CESM-Large Ensemble (CESM-LE) Project[34]. The ensemble mean of 40 members in CESM-LE Representative Concentration Pathway 8.5 (RCP 8.5) simulation has been

analyzed (Supplementary Fig. 7) to show the forced response due to rapidly increased greenhouse gas emissions in the early 21st century. The increased JJA Z200 can be found over the entire Arctic, but with a different spatial pattern and much smaller magnitudes compared to the observed one. Since all 40 members use the same model and external forcing, with only small round-off level differences in their initial conditions, their spread in Z200 linear trends can be attributed to the model's inherent internal variability[34]. The comparison between ERA-I and CESM-LE suggest that increased Z200 in the early 21st century is mainly induced by internal variability. This is consistent with the results in a previous study[12], although they use a longer record from 1979 to 2014. Due to the absence of anticyclonic circulation in the forced response, no significant linear trend of vertical velocity is found over the ocean in CESM-LE. In addition, CESM can capture the JJA temperature and humidity inversions as shown in ERA-I. However, the temperature inversion intensity in CESM-LE is much higher than that in reanalysis, particularly over
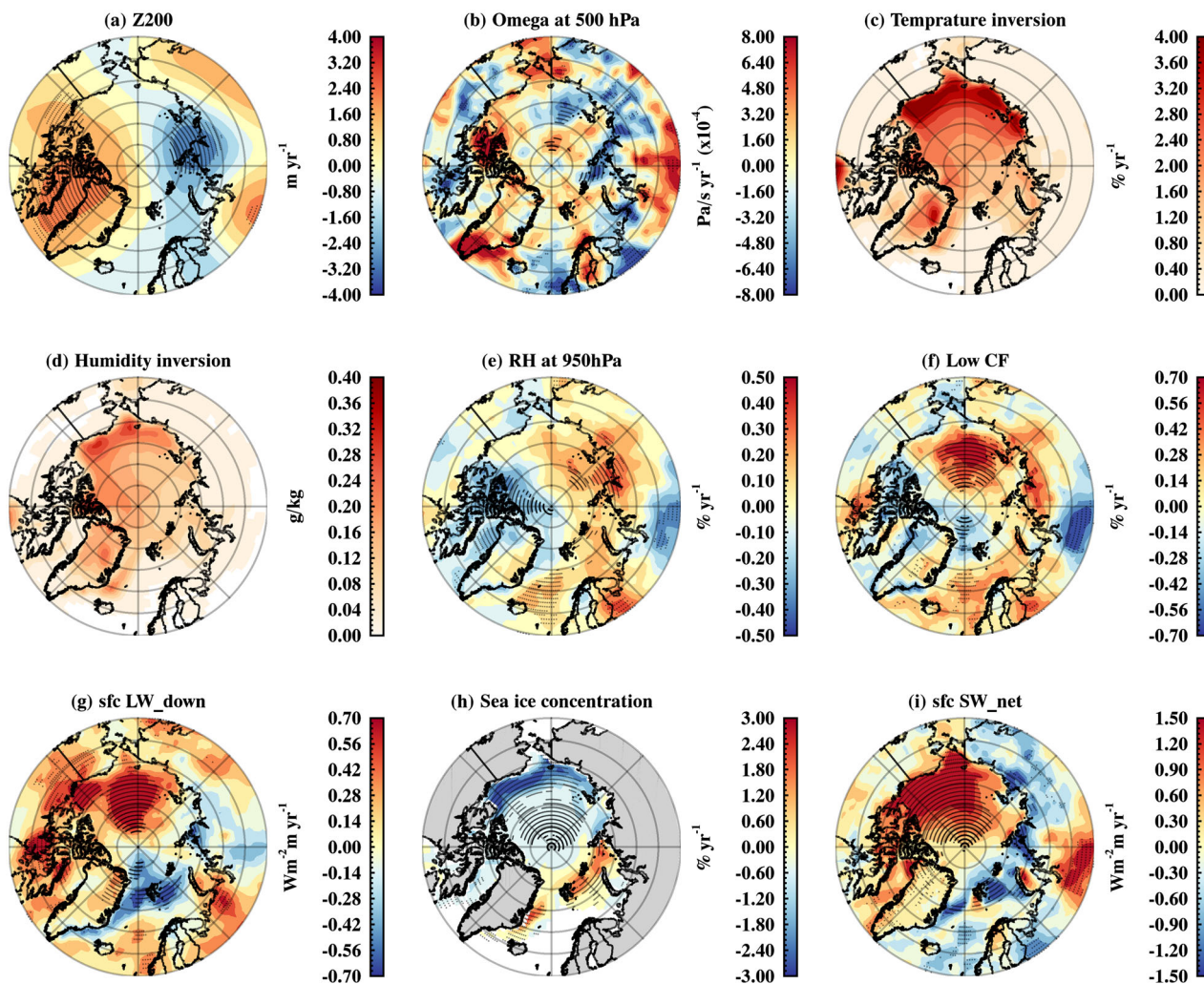
Fig. 3 The linear trend of summertime low clouds, large-scale circulation, and September Arctic sea ice from selected 20-year episodes in CESM preindustrial fully coupled simulation. a Linear trend of JJA geopotential height at 200 hPa (Z200). **b** Linear trend of JJA vertical velocity at 500 hPa. **c** Strength of JJA temperature inversion <900 hPa. **d** Strength of JJA humidity inversion <900 hPa. **e** Linear trend of JJA relative humidity at 950 hPa. **f** Linear trend of JJA low cloud fraction (CF, <700 hPa). **g** Linear trend of JJA downwelling longwave flux (LW_down) at the surface. **h** Linear trend of September sea ice concentration. **i** Linear trend of JJA net shortwave flux (SW_net) at the surface. The black dots indicate statistically significant linear trends at 10% significance level. The selected pseudo-ensemble member exhibiting the highest JJA Z200 pattern correlation ($r = 0.90$ at 1% significance level) with ERA-I based on fingerprint pattern matching method.

the Beaufort Sea, while the humidity inversion intensity is lower, especially over the East Siberian Sea. As for the RH at 950 hPa and low CF, the positive trends in CESM-LE are rather weak and not significant over the Arctic Ocean. The increased surface LW_down flux can be observed in the entire Arctic, but with smaller magnitudes. The changes in LW flux are more likely caused by the recent surface warming, as a result of anthropogenic forcing. Furthermore, the substantial sea ice decline shown here is believed to largely follow anthropogenic greenhouse gas emissions[35]. Interestingly, the CESM-LE does not capture the sea ice decline in the coastal regions as shown in observations. Moreover, the positive trend in net SW flux can also be found over the central Arctic Ocean, but with much smaller magnitudes. A comparison of observations with the forced response in CESM suggests that anthropogenic forcing is not sufficient to fully explain what has occurred in the Arctic in the past two decades and thus additional factors, such as large-scale circulation variability and low clouds should be carefully taken into account.

To determine whether the model exhibits internal variability that is similar to what has happened in the observations in terms of the circulation trends and their linkage to the surface, we analyze CESM-LE preindustrial simulation using a fingerprint pattern matching method[16,36]. Specifically, we partition the 1800-year preindustrial simulation into 1780 20-year-long pseudo-ensemble members[37]. The linear trend of JJA Z200 over the 20-year period is calculated for each member. Figure 3 shows the results from one member exhibiting the highest spatial correlation ($r = 0.90$ at 1% significance level) with ERA-I (Fig. 1b). By design, the linear trend of the JJA Z200 spatial pattern matches closely with that observed in the early 21st century (Fig. 3a), but with overall smaller magnitudes and a more prominent negative trend over the Laptev-Kara Sea. The JJA temperature (Fig. 3c) and humidity inversion intensities (Fig. 3d) show similar spatial patterns with ERA-I. Moreover, the majority of the Arctic Ocean exhibits positive trends in RH at 950 hPa, with the greatest signals over the Laptev and East Siberian Seas (Fig. 3e). As a result, the increased low CF (0.7% year^{-1}, Fig. 3f) and LW_down flux
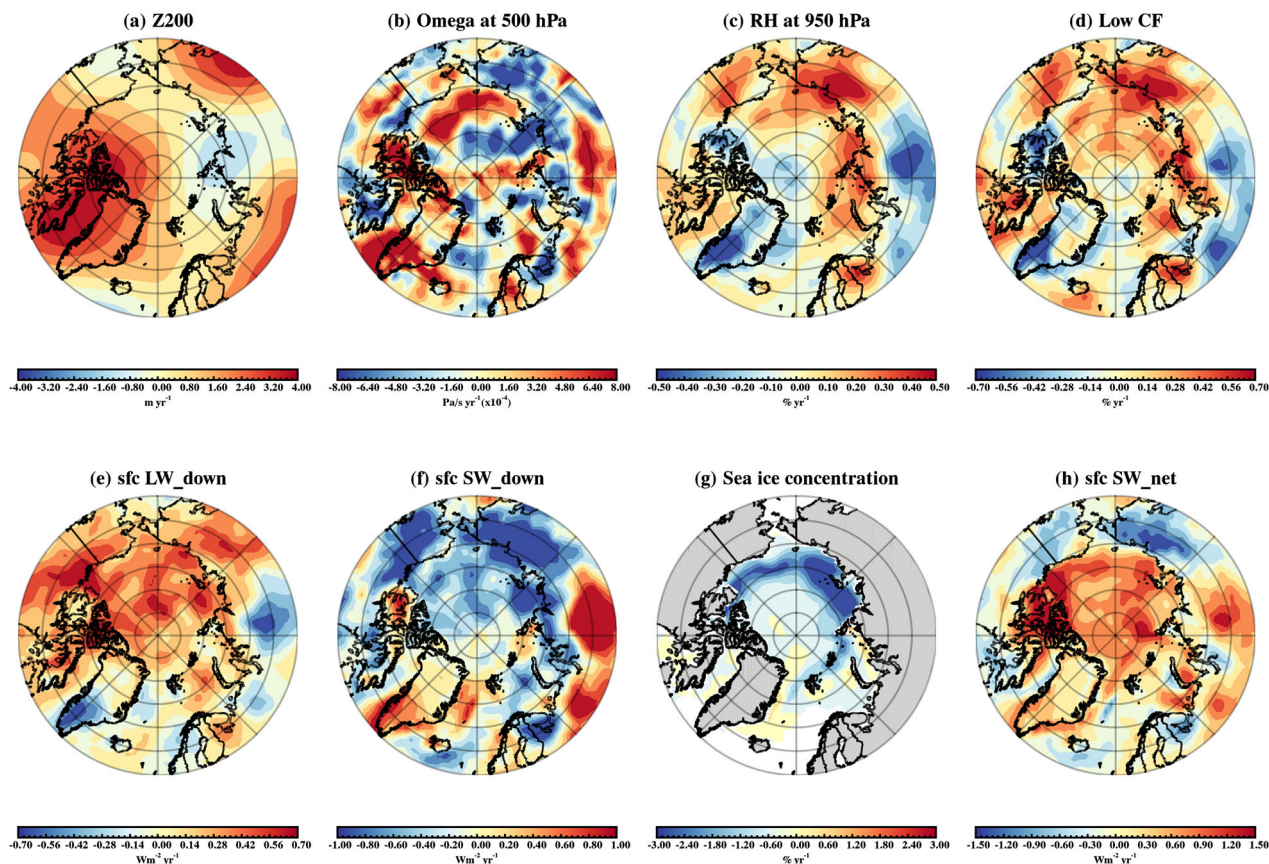
Fig. 4 The linear trend of summertime cloud and radiative properties and September Arctic sea ice during 2000–2016 from CESM nudging experiments. a Linear trend of JJA geopotential height at 200 hPa (Z200). **b** Linear trend of JJA vertical velocity at 500 hPa. **c** Linear trend of JJA relative humidity (RH) at 950 hPa. **d** Linear trend of JJA low cloud fraction (CF, <700 hPa). **e** Linear trend of JJA downwelling longwave flux (LW_down) at the surface. **f** Linear trend of JJA downwelling shortwave flux (SW_down) at the surface. **g** Linear trend of September sea ice concentration. **h** Linear trend of JJA net shortwave flux (SW_net) at the surface. All results are averaged from eight CESM nudging experiments.

$(0.7\ \mathrm{Wm^{-2}\ year^{-1}}$, Fig. 3g) occur mainly over the Chukchi and East Siberian Seas, with comparable magnitudes in observations (Fig. 1). The reduction of SW_down flux ($-1.2\ \mathrm{Wm^{-2}\ year^{-1}}$, not shown) can be found over the Beaufort, Chukchi, and East Siberian Seas, while the increase of SW_down flux occurs over the Greenland and Barents Seas, which match the regions seeing decreased low CF (Fig. 3f) and sea ice growth (Fig. 3h). Meanwhile, the sea ice has been retreating over the Pacific sector during this 20-year period (Fig. 3h). The SIC decline in this member has a similar magnitude ($-3\%\ \mathrm{year^{-1}}$) as in observations over the Beaufort Sea. As a result of increased low clouds and decreased sea ice, increased net SW flux (Fig. 3i) is found over the Chukchi and Beaufort Seas, with comparable magnitudes ($1.5\ \mathrm{Wm^{-2}\ year^{-1}}$) relative to observations. However, the stronger downward motion, which is believed to highly correlate with circulation changes in the upper troposphere, is not perfectly simulated by CESM (Fig. 3b) and is possibly due to stronger low pressure over the Laptev-Kara Sea compared to observations. Moreover, similar spatial patterns are found if we average the results from the best five nonoverlapping pseudo-ensemble members that own a high spatial correlation with the observed one, but with much smaller magnitudes (Supplementary Fig. 8).

Overall, CESM has some capabilities to capture the observed features over the Arctic when the observed circulation trend is captured well by chance. This high-pressure trend over north-eastern Canada and Greenland appears to be mostly internally driven, and thus does not rely on the presence of anthropogenic

forcing. However, some key mechanisms (e.g., vertical motion) that link large-scale circulation with other thermodynamical variables, cannot be fully reproduced by the model. Therefore, an atmospheric nudging experiment is necessary to further assess how low clouds and sea ice respond when observed winds are imposed in the model.

Atmospheric nudging experiments. To directly demonstrate the impacts of large-scale circulation, we conducted eight fully coupled simulations using CESM, in which the model's circulation in the Arctic (60°N northward) is partially nudged to the three-dimensional wind fields from 6-hourly ERA-I. Greenhouse gas concentrations are prescribed using year 2000 climatological values[38,39] to mute the impacts of global warming. Here, we only nudge the winds >860 hPa in model's hybrid sigma pressure coordinate to ERA-I because we would like to give the model some freedom to behave <860 hPa. We also conducted additional sensitivity experiments, in which the wind fields are nudged above different levels (820, 763, and 691 hPa). The results from these sensitivity experiments are quite consistent, indicating 860 hPa is reasonably selected. To ensure the reliability of our results, we integrate the model for two different lengths with very diverse initial conditions (see "Methods" section). Both sets show quite similar results so that the simulations over the period are quite stable and robust. Specifically, the global top-of-atmosphere (TOA) radiation imbalance of each simulation (Supplementary Fig. 9) is between 0.57 and $0.91\ \mathrm{Wm^{-2}}$ during 2000–2016, which

is close to estimates from CERES ($0.92\,Wm^{-2}$) and ERA-I ($0.69\,Wm^{-2}$), indicating the TOA energy budget in our simulations are reasonable and not disrupted.

Figure 4 shows the results averaged from eight ensemble members. The linear trend of JJA Z200 and vertical velocity at 500 hPa exhibit very similar spatial patterns as in ERA-I, since the CESM's zonal and meridional winds have been nudged to the reanalysis. Due to enhanced downward motion, increases in RH at 950 hPa (Fig. 4c) occur from the Laptev and East Siberian Seas to the Beaufort Sea. Compared to the preindustrial simulation, the magnitudes of the linear trends ($0.4\%\,year^{-1}$) in the nudging runs are closer to the satellite retrievals ($0.5\%\,year^{-1}$). More abundant moisture favors the formation of clouds, thus the increased low CF (Fig. 4d), enhanced LW_down (Fig. 4e), and decreased SW_down flux (Fig. 4f) can be found across nearly the entire Arctic Ocean. Note that the low CF ($0.7\%\,year^{-1}$) and LW_down flux ($0.7\,Wm^{-2}\,year^{-1}$) show comparable magnitude of changes relative to the observations, while the changes in SW_down flux ($-0.7\,Wm^{-2}\,year^{-1}$) are almost half of satellite retrievals ($-1.5\,Wm^{-2}\,year^{-1}$). As a response, the sea ice decreases with the strongest negative trend ($-3\%\,year^{-1}$) over the East Siberian Sea (Fig. 4g) and the surface albedo is decreased. Therefore, the absorbed solar radiation is increased (Fig. 4h, $1.5\,Wm^{-2}\,year^{-1}$) due to the ice-albedo feedback. Recall that the greenhouse gas concentrations remain constant for all nudging simulations, therefore, our results demonstrate the key role of summertime large-scale circulation in driving cloud changes and sea ice melt in the Arctic.

Discussion

Observations show that the decline of September SIC occurred along with increasing Z200 in summer during 2000–2016, which owns a strong internal origin. In the meantime, JJA low CF and associated LW CRE have been substantially increasing over the Beaufort and Chukchi Seas. The modeling studies suggest that the variability of RH and low CF is mainly driven by large-scale atmospheric circulation, particularly the changes in the upper troposphere. The increased low clouds facilitate sea ice melt underneath by emitting LW radiation and warming the lower troposphere. This forcing can also trigger the ice-albedo feedback, allowing more solar radiation to be retained by the ocean surface and further enhance sea ice melt. As a bridge between upper-level atmospheric circulation and the surface, the summertime low clouds eventually amplify the warming effect induced by stronger anticyclonic circulation over the Arctic.

Arctic clouds are generally believed to warm the surface during most of the year and cool the surface in summer[5,10,20,22]. By emphasizing low clouds, our study makes an advancement to this understanding. First, most of studies focus on total clouds[20–22] instead of low clouds, which are closer to the surface, and thus more efficient to regulate the surface temperature through the modulation of surface radiative fluxes[40]. Second, low clouds and high clouds may behave differently in controlling SW flux passing through. Overall, clouds may cool the surface for a very short time (~30 days) during the most intense summer ice melt, due to its high cloud albedo[22]. However, low clouds must work with the surface to determine how much solar radiation could reach the surface. We do see a decrease in JJA SW_down flux during 2000–2016 (Supplementary Fig. 5), which can compensate the increased LW_down flux in summer. In addition to low clouds, the surface albedo also exerts a large influence on the SW_down flux, particularly in the polar regions. With ice melt, the decreased SW_down flux could be in part explained by a reduction in multiple reflections between clouds and surface[41]. This can be demonstrated by the strong positive pattern correlations between

SIC and SW_down flux in June and July (0.57 and 0.65 at 1% significance level). Nevertheless, we cannot rule out the possibility that increased low-level clouds may cool the surface through reducing SW_down flux. However, how much of the cloud warming effect can be compensated by the cloud cooling effect remains an open question and needs further investigation.

Our study thus highlights the importance of Arctic summertime low clouds in linking large-scale atmospheric circulation and sea ice variations. Based on model simulations, the Arctic is projected to become cloudier under greenhouse forcing in a warmer world due to newly open water[32]. However, how sea ice will behave in the future remains a difficult question, since it is very uncertain how climate models reproduce the observed circulation–cloud–sea ice relationship. Therefore, our study suggests that accurately simulating summertime large-scale circulation, as well as the cloud response to circulation, is a critical step toward increasing the reliability of seasonal sea ice forecasts and the rate of future sea ice loss.

Methods

Datasets and model experimental design. Monthly SIC and extent are obtained from Nimbus-7 SSMR and DMSP SSM/I-SSMIS passive microwave data version-1 provided by the National Snow and Ice Data Center[42]. SIC is derived from surface brightness temperatures measured from the following sensors: Nimbus-7 SMMR, the DMSP-F8, -F11, and -F13 SSM/I, and the DMSP-F17 SSMIS. The data is provided in the polar stereographic projection with a grid cell size of 25 km × 25 km in polar stereographic grid from October 1978 to present. The uncertainty of SIC over the Arctic is within ±5% during the winter and increases to ±15% during the summer when melt ponds are present on the sea ice[43]. Note that the sea ice extent is computed as the total area in the Arctic with SIC >15% at each grid box. The conversion of SIC to sea ice extent is conducted at the daily timescale.

ERA-I is produced with the European Centre for Medium-Range Weather Forecasts (ECMWF)'s Integrated Forecast System, a forecast model with three fully coupled components for the atmosphere, land surface, and ocean waves. In addition, the 12-hourly four-dimensional (4D) variational data assimilation (4D-Var) of the upper-air atmospheric state is the key component of its data assimilation system[44]. The ERA-I product contains 60 model levels with the highest level being 0.1 hPa, and the horizontal resolution is T255 (nominally 0.70°). The ERA-I product has been evaluated over the Arctic in the previous studies, including surface temperature, radiative fluxes, precipitation, wind speed, and cloud properties[45,46]. It was found that the ERA-I reanalysis stands out among several global reanalysis products as being more consistent with independent observations.

Cloud properties used in this study are from the CERES Moderate Resolution Imaging Spectroradiometer (MODIS) SYN1deg Edition 4.1 (Ed4.1) monthly gridded dataset (1° × 1°) from 2000 to 2016, which is derived from both Aqua and Terra satellite measurements[17]. For Ed4, the CERES project has taken advantage of the next-generation geostationary satellite (GEO) imager capabilities rather than relying solely on first-generation GEO cloud retrievals. In addition, both the MODIS and GEO cloud retrieval algorithms were significantly improved compared to Edition 3A (ref. [47]). A previous study found that there is a global 7% uncertainty in CERES-MODIS Aqua and Terra CF retrievals[48]. In the Arctic, monthly mean CFs from CERES SYN1deg have almost identical values (within ±2%) with active remote sensing product CALIPSO in summer[46]. Specifically, the CERES SYN1deg Ed4A low CF (>700 hPa) is generally consistent with the low CF (<3 km) from in situ measurements at Atmospheric Radiation Measurement Program Northern Slope of Alaska (71.33°N–156.61°) site (Supplementary Fig. 10). As suggested by the CERES team, the Terra or Aqua SSF1deg Ed4A MODIS-retrieved cloud properties are of climate quality and can be used to determine long-term regional cloud trends[47]. Therefore, we also compare the linear trend of low CF between SYN1deg Ed4.1 and Terra/Aqua SSF1deg Ed4.1 product. The Aqua SSF1deg product exhibits almost the same spatial pattern (Supplementary Fig. 11), as shown in the SYN1deg product. The Terra SSF1deg Ed4.1 product also shows a similar spatial distribution (Supplementary Fig. 11) as SYN1deg with the greatest positive trend over the AOF, but the magnitude is much smaller than SYN1deg and Aqua SSF1deg products. Since either Terra or Aqua SSF1deg products do not encompass the entire diurnal cycle, we still focus on the SYN1deg in the main text.

The surface radiative fluxes are obtained from CERES-EBAF Surface Ed4.1 datasets, with a monthly temporal scale and 1° × 1° spatial resolution. EBAF surface fluxes were calculated using the Langley modified Fu-Liou radiative transfer model with inputs from MODIS-retrieved cloud properties, meteorological data from a reanalysis system, and aerosol data from an aerosol assimilation system[49]. The EBAF Surface Ed4 monthly mean downward irradiances have been evaluated using surface measurements at 46 buoys and 36 land sites[50], and concluded that mean biases of SW_down and LW_down irradiances averaged for all sites are smaller than $5\,Wm^{-2}$. Specifically, by comparing four surface sites over the Arctic, the

regional biases (root-mean-square differences) are +3.6 (13.0) Wm^{-2} for SW_down flux and +0.2 (12.3) Wm^{-2} for LW_down flux. Previous studies concluded that CERES-EBAF surface fluxes should be considered as a key benchmark for evaluating the Arctic surface radiation budget[46,51,52].

This study also uses vertical profiles of RH from Atmospheric Infrared Sounder (AIRS)/Aqua level 3 version 6 monthly standard physical retrieval product[53]. The AIRS is a grating spectrometer ($R = 1200$) aboard the second Earth Observing System (EOS) polar-orbiting platform, EOS Aqua. In combination with the Advanced Microwave Sounding Unit and the Humidity Sounder for Brazil, AIRS constitutes an innovative atmospheric sounding group of visible, infrared, and microwave sensors[54]. The data were obtained from NASA Goddard Earth Sciences Data and Information Services Center with 1˚ × 1˚ spatial resolution from 2003 to 2016. Note that we use the vertical structure of RH from ERA-I in Fig. 2c, f, because the vertical resolution of AIRS is too coarse (12 vertical levels). In addition, both ERA-I and AIRS can capture the positive trend of RH in the lower troposphere over the AOF (Supplementary Fig. 12). However, ERA-I cannot well capture the increasing trend of RH over the AOF in terms of spatial distribution (Supplementary Fig. 12). Therefore, the spatial pattern in Fig. 2i is based on AIRS instead of ERA-I.

As for model simulations, we use CESM-LE for analysis. As a comprehensive resource for studying climate change in the presence of internal climate variability, the CESM-LE is run with fully coupled atmosphere, ocean, land, and sea ice components from 1920 to 2100. Forty ensemble members are simulated that use the same model and external forcing, but with small round-off level variations in their air temperature initial conditions[34]. In this study, we used the monthly mean output from Community Atmosphere Model version 5 (CAM5), which is provided in a grid of 0.94° (latitude) × 1.25° (longitude). Here, we mainly focus on 1800 years of preindustrial (1850) fully coupled simulation and 40 ensemble members from RCP 8.5 simulation in CESM-LE project[34].

Overall, CESM can capture general Arctic temperature, humidity, cloud, radiation, and sea ice features[34,55]. Particularly, the CESM simulated seasonal cycle of Arctic sea ice extent matches very well with observations in the late 20th century. The spatial distribution of sea ice thickness is also in a good agreement with observations[55]. In addition, CAM5 simulated Arctic CF is biased as twice as much winter cloud as the CALIPSO satellite observations[6,56]. In the meantime, CAM5 has too few liquid clouds in the Arctic[57]. Therefore, it is not surprising that CESM-LE underestimates LW_down flux and overestimate SW_down flux at the surface. And the model represents the spatial pattern of surface LW_down flux fairly well, but the magnitude is consistently too low[57].

In this study, we use CESM1.2.2.1 (ref. [55]) for the nudging experiments. As a participant in CMIP5, CESM1 is a fully coupled community GCM, which simulates climate states for Earth's past, present, and future. All simulations are conducted in National Center for Atmospheric Research (NCAR)'s supercomputer, Cheyenne. The CAM5 is run using the finite volume dynamical core with the standard ~0.9˚ × 1.25˚ horizontal grid and 30 vertical levels. Details about dynamics and model physics for CAM5 can be found in the NCAR technical note[58]. The land model is run with the same horizontal resolution as the atmosphere model. Moreover, the ocean and sea ice models use the displaced pole gx1v6 grid.

We completed eight simulations, in which the atmospheric circulations in the Arctic (60˚ N northward) are nudged to the 3D wind fields (zonal and meridional winds at different vertical levels) from ERA-I 6-hourly winds (zonal and meridional). The strength of nudging is set to 0.5 (0 indicates no nudging and 1 means to replace the model's wind fields with observations completely) for all experiments, allowing the model to generate its own dynamical fields to some extent[12]. We find that our result is not sensitive to this nudging strength if it is set >0.5. In addition, we only nudged the winds >860 hPa in model's hybrid sigma pressure coordinate to the reanalysis because we would like to give the model some freedom to behave <860 hPa, in which observations show an increasing trend of low clouds. Greenhouse gas concentrations are prescribed using year 2000 climatological values[38,39]. Note that the first four experiments (Exp-1 to Exp-4) are run from 1979 to 2016 and the results before 2000 are considered as "spin-up" and thus discarded from analysis. The last four experiments (Exp-5 to Exp-8) are run from 2000 to 2016. The results from both sets are relatively stable after 2000 in terms of global TOA radiation imbalance. To examine how sensitive the simulations are to the initial states, we use very diverse initial sea ice conditions for the last four experiments. The results from each individual member indicate that the responses of low clouds (Supplementary Fig. 13) and sea ice (Supplementary Fig. 14) to atmospheric circulation are quite consistent and robust, although slight regional differences are found across those members. Additional details on our experimental design are introduced in Supplementary Table 1.

Exp-1: Default initial conditions for B_2000_CAM5_CN component set; the atmospheric circulations in the Arctic are nudged to the ERA-I wind (u,v) fields from 860 hPa to the TOA during 1979–2016; the results during 2000–2016 are analyzed.

Exp-2: Same as Exp-1, except that circulations are nudged from surface to the TOA.

Exp-3: Same as Exp-1, except that we use initial conditions from year 2000 in CESM-LE historical simulation member 23 (b.e11.B20TRC5CNBDRD. f09_g16.023); this member shows the largest Arctic sea ice area among member 1–30.

Exp-4: Same as Exp-1, except that we use initial conditions from year 2000 in CESM-LE historical simulation member 22 (b.e11.B20TRC5CNBDRD. f09_g16.022); this member shows the smallest Arctic sea ice area among member 1–30.

Exp-5: Same as Exp-3, except that the simulation is only performed during 2000–2016.

Exp-6: Same as Exp-4, except that the simulation is only performed during 2000–2016.

Exp-7: Same as Exp-5, except that we use initial conditions from year 2000 in CESM-LE historical simulation member 14 (b.e11.B20TRC5CNBDRD. f09_g16.014); this member shows the highest Arctic sea ice volume among member 1–30.

Exp-8: Same as Exp-6, except that we use initial conditions from year 2000 in CESM-LE historical simulation member 20 (b.e11.B20TRC5CNBDRD. f09_g16.020); this member shows the second lowest Arctic sea ice volume among member 1–30; it provides a reasonable comparison to Exp-7 because the ensemble member 14 and 20 shows the substantial contrast on sea ice volume, but with similar sea ice area values.

Statistical analyses. The MCA analysis is used to identify patterns in two space-time datasets, which explain a maximum fraction of the covariance between them[59,60]. Here, we applied MCA to space-time data for JJA Z200 (60˚N northward) from ERA-I and JJA low CF (70˚ northward) during 2000–2016. Specifically, the MCA uses singular value decomposition of a covariance matrix between Z200 and low CF. The leading patterns show the time series and spatial patterns of the two fields that are optimally coupled.

To test the statistical significance of correlations, we use effective sample size N^* by considering the impact of secular trend on the correlation[61], which is given by

$$N^* = N \frac{1 - r_1 r_2}{1 + r_1 r_2} \qquad (1)$$

Where N is the number of available time steps, and r_1 and r_2 are lag-one autocorrelation coefficients of each variable. A significance level 10% ($\alpha = 0.1$) is used in this study to determine the significance of correlation.

Data availability

Sea Ice Concentrations from Nimbus-7 SMMR and DMSP SSM/I-SSMIS Passive Microwave Data, Version 1 is accessed from NASA DAAC at the National Snow and Ice Data Center at http://nsidc.org/data/docs/daac/nsidc0051_gsfc_seaice.gd. html#cavalieri_92. The ECMWF ERA-Interim reanalysis product is available at https:// www.ecmwf.int/en/forecasts/datasets/reanalysis-datasets/era-interim. NASA AIRS/Aqua L3 monthly standard physical retrieval version 6 can be obtained from https://disc.gsfc. nasa.gov/datasets/AIRS3STM_006/summary?keywords=AIRS%20L3. NASA CERES SYN1deg and CERES-EBAF surface datasets are available at http://ceres.larc.nasa.gov/. The output of CESM-Large Ensemble project is available on NCAR Climate Data Gateway (https://www.earthsystemgrid.org/dataset/ucar.cgd.ccsm4. CESM_CAM5_BGC_LE.html). The data generated for this paper can be accessed via https://doi.org/10.17605/OSF.IO/MSC7W. In addition, the CESM atmospheric nudging experiment raw output is available from the corresponding author upon request.

References

1. Notz, D. & Stroeve, J. C. The trajectory towards a seasonally ice-free Arctic Ocean. *Curr. Clim. Change Rep.* **4**, 407–416 (2018).
2. Kwok, R. & Rothrock, D. A. Decline in Arctic sea ice thickness from submarine and ICESat records: 1958–2008. *Geophys. Res. Lett.* **36**, 1958–2008 (2009).
3. IPCC. In *IPCC Special Report on the Ocean and Cryosphere in a Changing Climat* (ed. Pörtner, H.-O. et al) (2019).
4. Kapsch, M. L., Graversen, R. G. & Tjernström, M. Springtime atmospheric energy transport and the control of Arctic summer sea-ice extent. *Nat. Clim. Change* **3**, 744–748 (2013).
5. Kay, J. E. & Gettelman, A. Cloud influence on and response to seasonal Arctic sea ice loss. *J. Geophys. Res. Atmos.* **114**, D18204 (2009).
6. Kay, J. E. et al. Recent advances in Arctic cloud and climate research. *Curr. Clim. Change Rep.* **2**, 159–169 (2016).
7. Dong, X. et al. Critical mechanisms for the formation of extreme arctic sea-ice extent in the summers of 2007 and 1996. *Clim. Dyn.* **43**, 53–70 (2014).
8. Cesana, G., Kay, J. E., Chepfer, H., English, J. M. & De Boer, G. Ubiquitous low-level liquid-containing Arctic clouds: new observations and climate model constraints from CALIPSO-GOCCP. *Geophys. Res. Lett.* **39**, L20804 (2012).

9. Curry, J. A., Ebert, E. E. & Herman, G. F. Mean and turbulence structure of the summertime Arctic cloudy boundary layer. *Q. J. R. Meteorol. Soc.* **114**, 715–746 (1988).

10. Dong, X. et al. A 10-yr climatology of arctic cloud fraction and radiative forcing at Barrow, Alaska. *J. Geophys. Res. Atmos.* **115**, D17212 (2010).

11. Huang, Y. et al. Thicker clouds and accelerated Arctic sea ice decline: the atmosphere-sea ice interactions in spring. *Geophys. Res. Lett.* **46**, 6980–6989 (2019).

12. Ding, Q. et al. Influence of high-latitude atmospheric circulation changes on summertime Arctic sea ice. *Nat. Clim. Change* **7**, 289–295 (2017).

13. Kay, J. E., L'Ecuyer, T., Gettelman, A., Stephens, G. & O'Dell, C. The contribution of cloud and radiation anomalies to the 2007 Arctic sea ice extent minimum. *Geophys. Res. Lett.* **35**, L08503 (2008).

14. Kay, J. E. & L'Ecuyer, T. 2013. Observational constraints on Arctic Ocean clouds and radiative fluxes during the early 21st century. *J. Geophys. Res. Atmos.* **118**, 7219–7236 (2013).

15. Perovich, D. K. et al. Increasing solar heating of the Arctic Ocean and adjacent seas, 1979–2005: attribution and role in the ice-albedo feedback. *Geophys. Res. Lett.* **34**, L19505 (2007).

16. Baxter, I. et al. How tropical Pacific surface cooling contributed to accelerated sea ice melt from 2007 to 2012 as ice is thinned by anthropogenic forcing. *J. Clim.* **32**, 8583–8602 (2019).

17. Wettstein, J. J. & Deser, C. Internal variability in projections of twenty-first-century Arctic sea ice loss: role of the large-scale atmospheric circulation. *J. Clim.* **27**, 527–550 (2014).

18. DeWeaver, E. & Bitz, C. M. Atmospheric circulation and its effect on Arctic sea ice in CCSM3 simulations at medium and high resolution. *J. Clim.* **19**, 2415–2436 (2006).

19. Wielicki, B. A. et al. Clouds and the earth's radiant energy system (CERES): an earth observing system experiment. *Bull. Amer. Meteor. Soc.* **77**, 853–868 (1996).

20. Shupe, M. D. & Intrieri, J. M. Cloud radiative forcing of the Arctic surface: the influence of cloud properties, surface albedo, and solar zenith angle. *J. Clim.* **17**, 616–628 (2004).

21. Choi, Y. et al. Effect of Arctic clouds on the ice-albedo feedback in midsummer. *Int. J. Climatol.* **40**, 4707–4714 (2020).

22. Intrieri, J. M. et al. An annual cycle of Arctic surface cloud forcing at SHEBA. *J. Geophys. Res. Oceans* **107**, 8039 (2002).

23. Wendler, G., Moore, B., Hartmann, B., Stuefer, M. & Flint, R. Effects of multiple reflection and albedo on the net radiation in the pack ice zones of Antarctica. *J. Geophy. Res. Atmos.* **109**, D06113 (2004).

24. Qiu, S., Dong, X., Xi, B. & Li, J. L. Characterizing Arctic mixed-phase cloud structure and its relationship with humidity and temperature inversion using ARM NSA observations. *J. Geophys. Res. Atmos.* **120**, 7737–7746 (2015).

25. Solomon, A., Shupe, M. D., Persson, P. O. G. & Morrison, H. Moisture and dynamical interactions maintaining decoupled Arctic mixed-phase stratocumulus in the presence of a humidity inversion. *Atmos. Chem. Phys.* **11**, 10127–10148 (2011).

26. Solomon, A. et al. The sensitivity of springtime Arctic mixed-phase stratocumulus clouds to surface-layer and cloud-top inversion-layer moisture sources. *J. Atmos. Sci.* **71**, 574–595 (2014).

27. Herman, G. & Goody, R. Formation and persistence of summertime Arctic stratus clouds. *J. Atmos. Sci.* **33**, 1537–1553 (1976).

28. Klein, S. A. & Hartmann, D. L. The seasonal cycle of low stratiform clouds. *J. Clim.* **6**, 1587–1606 (1993).

29. Tsay, S. C. & Jayaweera, K. O. L. F. Physical characteristics of Arctic stratus clouds. *J Appl. Meteorol. Clim.* **23**, 584–596 (1984).

30. Tjernström, M. et al. 2014. The Arctic Summer Cloud Ocean Study (ASCOS): overview and experimental design. *Atmos. Chem. Phys.* **14**, 2823–2869 (2014).

31. Morrison, A. L., Kay, J. E., Chepfer, H., Guzman, R. & Yettella, V. Isolating the liquid cloud response to recent Arctic sea ice variability using spaceborne lidar observations. *J. Geophys. Res. Atmos.* **123**, 473–490 (2018).

32. Vavrus, S., Waliser, D., Schweiger, A. & Francis, J. Simulations of 20th and 21st century Arctic cloud amount in the global climate models assessed in the IPCC AR4. *Clim. Dyn.* **33**, 1099 (2009).

33. Taylor, P. C., Kato, S., Xu, K. M. & Cai, M. Covariance between Arctic sea ice and clouds within atmospheric state regimes at the satellite footprint level. *J. Geophys. Res. Atmos.* **120**, 12656–12678 (2015).

34. Kay, J. E. et al. The Community Earth System Model (CESM) large ensemble project: a community resource for studying climate change in the presence of internal climate variability. *Bull. Am. Meteor. Soc.* **96**, 1333–1349 (2015).

35. Notz, D. & Stroeve, J. Observed Arctic sea-ice loss directly follows anthropogenic CO2 emission. *Science* **354**, 747–750 (2016).

36. Ding, Q. et al. Fingerprints of internal drivers of Arctic sea ice loss in observations and model simulations. *Nat. Geosci.* **12**, 28–33 (2019).

37. Rosenblum, E. & Eisenman, I. Sea ice trends in climate models only accurate in runs with biased global warming. *J. Clim.* **30**, 6265–6278 (2017).

38. Lamarque, J. -F. et al. Historical (1850–2000) gridded anthropogenic and biomass burning emissions of reactive gases and aerosols: Methodology and application. *Atmos. Chem. Phys.* **10**, 7017–7039 (2010).

39. Liu, X. et al. Toward a minimal representation of aerosols in climate models: description and evaluation in the Community Atmosphere Model CAM5. *Geosci. Model Dev.* **5**, 709–739 (2012).

40. Sedlar, J. et al. A transitioning Arctic surface energy budget: the impacts of solar zenith angle, surface albedo and cloud radiative forcing. *Clim. Dyn.* **37**, 1643–1660 (2011).

41. Wendler, G., Eaton, F. D. & Ohtake, T. Multiple reflection effects on irradiance in the presence of Arctic stratus clouds. *J. Geophys. Res. Oceans* **86**, 2049–2057 (1981).

42. Cavalieri, D. J., Parkinson, C., Gloersen, P. & Zwall H. J. *Sea Ice Concentrations from Nimbus-7 SMMR and DMSP SSM/I-SSMIS Passive Microwave Data, Version 1* (NASA DAAC at the National Snow and Ice Data Center, 1996).

43. Cavalieri, D. J. et al. *NASA Sea Ice Validation Program for the DMSP SSM/I: Final Report, NASA Technical Memorandum 104559*, 126 (National Aeronautics and Space Administration, 1992).

44. Dee, D. P. et al. The ERA-Interim reanalysis: Configuration and performance of the data assimilation system. *Q. J. R. Meteorol. Soc.* **137**, 553–597 (2011).

45. Lindsay, R., Wensnahan, M., Schweiger, A. & Zhang, J. Evaluation of seven different atmospheric reanalysis products in the Arctic. *J. Clim.* **27**, 2588–2606 (2014).

46. Huang, Y. et al. Quantifying the uncertainties of reanalyzed arctic cloud and radiation properties using satellite surface observations. *J. Clim.* **30**, 8007–8029 (2017).

47. CERES. CERES_SYN1deg_Ed4A Data Quality Summary https://ceres.larc.nasa.gov/documents/DQ_summaries/CERES_SYN1deg_Ed4A_DQS.pdf (2017).

48. Minnis, P. et al. Cloud detection in non-polar regions for CERES using TRMM VIRS and Terra 615 and Aqua MODIS data. *IEEE Trans. Geosci. Remote Sens.* **46**, 3857–3884 (2008).

49. Kato, S. et al. Surface irradiances consistent with CERES-derived top-of-atmosphere shortwave and longwave irradiances. *J. Clim.* **26**, 2719–2740 (2013).

50. Kato, S. et al. Surface irradiances of edition 4.0 clouds and the earth's radiant energy system (CERES) energy balanced and filled (EBAF) data product. *J. Clim.* **41**, 4501–4527 (2018).

51. Boeke, R. C. & Taylor, P. C. 2016: Evaluation of the Arctic surface radiation budget in CMIP5 models. *J. Geophys. Res. Atmos.* **121**, 8525–8548 (2016).

52. Christensen, M. W. et al. Arctic observation and reanalysis integrated system: a new data product for validation and climate study. *Bull. Am. Meteorol. Soc.* **97**, 907–916 (2016).

53. Kahn, B. H. et al. The atmospheric infrared sounder version 6 cloud products. *Atmos. Chem. Phys.* **13**, 14477–14543 (2013).

54. Susskind, J., Blaisdell, J. M. & Iredell, L. Improved methodology for surface and atmospheric soundings, error estimates, and quality control procedures: the atmospheric infrared sounder science team version-6 retrieval algorithm. *J. Appl. Rem. Sens.* **8**, 084994 (2014).

55. Hurrell, J. W. et al. The community earth system model: a framework for collaborative research. *Bull. Amer. Meteor. Soc.* **94**, 1339–1360 (2013).

56. Kay, J. E. et al. Exposing global cloud biases in the Community Atmosphere Model (CAM) using satellite observations and their corresponding instrument simulators. *J. Clim.* **25**, 5190–5207 (2012).

57. McIlhattan, E. A., L'Ecuyer, T. S. & Miller, N. B. Observational evidence linking arctic supercooled liquid cloud biases in CESM to snowfall processes. *J. Clim.* **30**, 4477–4495 (2017).

58. Neale, R. B. et al. Description of the NCAR Community Atmosphere Model (CAM 5.0). NCAR Tech. Note NCAR/TN-4861STR http://www.cesm.ucar.edu/models/cesm1.0/cam/docs/description/cam5_desc.pdf (2010).

59. Bretherton, C. S., Smith, C. & Wallace, J. M. An intercomparison of methods for finding coupled patterns in climate data. *J. Clim.* **5**, 541–560 (1992).

60. Wallace, J. M., Smith, C. & Bretherton, C. S. Singular value decomposition of wintertime sea surface temperature and 500-mb height anomalies. *J. Clim.* **5**, 561–576 (1992).

61. Bretherton, C. S., Widmann, M., Dymnikov, V. P., Wallace, J. M. & Bladé, I. The effective number of spatial degrees of freedom of a time-varying field. *J. Clim.* **12**, 1990–2009 (1999).

Acknowledgements

Author contributions

Y.H. carried out all the analyses and conducted CESM simulations, made all the figures and wrote the paper; Q.D. conceived the main idea for CESM experimental design, as well as conducted CESM simulations; X.D. provided crucial guidance in interpretation of observational and modeling results; B.X. participated in constructive discussions, and contributed to interpretation of observational and modeling results; I.B. participated in constructive discussions, and contributed to interpreting results and writing the paper.

Competing interests

The authors declare no competing interests.

Additional information

Supplementary information The online version contains supplementary material available at https://doi.org/10.1038/s43247-021-00114-w.

Correspondence and requests for materials should be addressed to Q.D.

Peer review information Primary handling editor: Heike Langenberg

Reprints and permission information is available at http://www.nature.com/reprints

Publisher's note Springer Nature remains neutral with regard to jurisdictional claims in published maps and institutional affiliations.